Design of a Highly Sensitive Self-Reference Tamm-Plasmon-Polariton Sensor Employing Ti_3C_2Tx MXene

Abinash Panda, *Graduate Student Member, IEEE*, Puspa Devi Pukhrambam, *Member, IEEE*, and Joni Welman Simatupang, *Senior Member, IEEE*

***Abstract*—This paper presents design and analysis of a self-reference refractive index sensor for precise detection of different concentrations of H5N1 virus in poultry. The sensor is based on the study of Tamm plasmon polariton (TPP) modes excited between Ti_3C_2Tx MXene and cavity layer integrated 1D photonic crystal (PhC). We demonstrate the self-reference characteristics of the sensor, which significantly decreases the error contributions by the environmental factors like the light intensity fluctuations and local temperature variations. The transfer matrix method (TMM) is employed to investigate the reflectance and absorbance of the sensor. The cornerstone of this work lies on the assay of the shift in the wavelength and intensity of the TPP mode vis-à-vis different concentrations of the H5N1 virus. Numerous structural parameters like selection of materials, thickness of the MXene layer, thickness of the cavity layer, and period of the PhC are judiciously optimized to envisage maximum sensing performance. The colormap plot of field distribution infers a strong electric field localization in the cavity layer, which indicates high absorption of TPP modes. Compared to the traditional TPP sensor designed with Ag thin film, the electric field intensity (EFI) and sensitivity of the proposed MXene-based TPP sensor have been boosted by 40% and 15.93% respectively. It is appraised that the proposed sensor delivers a maximum sensitivity of 60.9375 nm/HAU, quality factor of 5485.71, and detection limit of 2.6×10^{-6} RIU. The proposed sensor can find suitable applications in the field of biomedical diagnostics, healthcare, food safety, and environmental monitoring.**

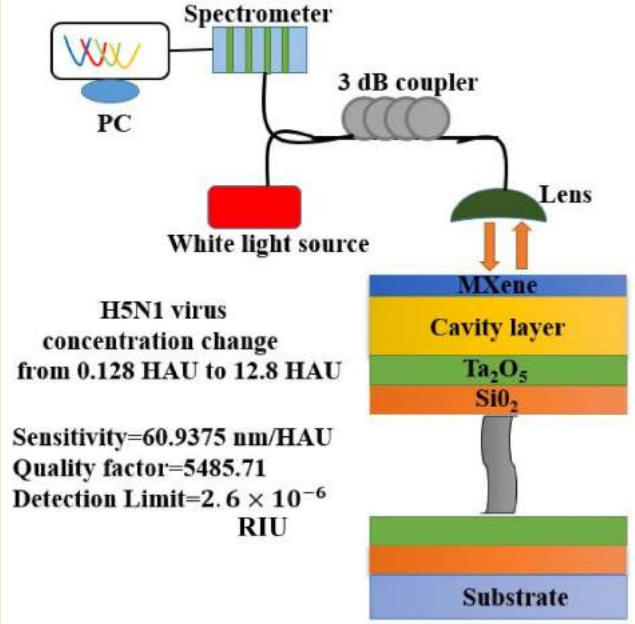

***Index Terms*—Tamm plasmon polariton, Ti_3C_2Tx MXene material, sensors, TMM, sensitivity.**

I. Introduction

AVIAN influenza, commonly known as bird-flue, is an infectious threat in the poultry sector. Bird-flue is resulted by type-A avian influenza virus (AIV), which causes substantial financial damage across the globe [1], [2]. In early 1997, Hong Kong was affected by AIV H5N1 as the first country, where 18 infections and 6 deaths were reported [3], [4]. Afterwards, H5N1 virus has been detected in many countries around the world, particularly in the Asia, Africa, and Europe countries. The continuously increasing death rate has driven attentions among the researchers to develop numerous techniques for the detection of AIV H5N1 in humans and animals. Nowadays, many technologies are available to diagnose AIV infections, such as serological analysis, polymerase chain reaction (PCR), in vitro virus isolation through culture. The serological technique shows less sensitivity towards detection of diverse AIV [5], in vitro virus isolation through culture consumes more time. Although, the PCR-based detection is more sensitive, but this technique is unable to discriminate the live viruses from inactivated viruses [6]. Above all, the aforesaid methods require highly sophisticated lab facilities

Manuscript received May 13, 2022; accepted May 15, 2022. Date of publication May 18, 2022; date of current version July 1, 2022. This work was supported by the Science and Engineering Research Board (SERB), Department of Science and Technology (DST), Government of India, under Grant EEQ/2021/000575. The associate editor coordinating the review of this article and approving it for publication was Prof. Carlos Marques. *(Corresponding author: Abinash Panda.)*

Abinash Panda and Puspa Devi Pukhrambam are with the Department of Electronics and Communication Engineering, National Institute of Technology Silchar, Silchar, Assam 788010, India (e-mail: abinashpanda087@gmail.com; puspa.devi@ece.nits.ac.in).

Joni Welman Simatupang is with the Department of Electrical Engineering, President University, Cikarang Utara, Bekashi Regency, West Java 17530, Indonesia (e-mail: joniwsmtp@president.ac.id).

Digital Object Identifier 10.1109/JSEN.2022.3175960

and highly skilled lab technicians [7]. To overcome these limitations, it is essential to develop a label-free sensor for quick and accurate detection of AIV H5N1 virus.

Tamm plasmon polariton (TPP), first introduced in 2007, is regarded as a unique form of surface modes that can be stimulated at the interface of two dissimilar mediums at normal incidence. When light (photons) strike on the metal, the electrons are dislocated and move in a wave like motion, which is known as plasmon waves [8]. The plasmon waves are localized in the interface of metal and cavity layer. At a certain incident angle, the resonance condition is achieved, where the reflectivity attains a minimum value. This resonant mode is also known as Tamm plasmon polariton mode [9]. TPP evolves as an appropriate alternative to the conventional surface plasmon polariton (SPP) by offering a propitious platform to combine simple geometry and ultrahigh sensitivity. It is worth mentioning that, opposed to SPP, stimulation of TPP does not need to satisfy the total reflection condition and can be observed for both TE (transverse electric) and TM (transverse magnetic) polarization modes at any incident angle. A light wave when the electric field vector lies in the incidence plane is known as TM mode or called p- polarized light, and a light wave which the electric field vector lies normal to the incidence plane is called TE or s-polarized light. Both TE and TM-polarized TPP modes facilitate ease of excitation of plasmonic waves along with interesting dispersive features in comparison to SPP-modes [10].

Klimov *et al.* demonstrated the coupling of the optical Tamm state with waveguide modes via a periodic array of slits. The authors studied the transmittance spectrum to detect the change in the environmental refractive index [11]. Leitao *et al.* experimentally developed a highly sensitive cortisol immunosensor by using SPR and POD (plastic optical fiber) technology. They detected cortisol concentrations in the range 0.005 to 10 ng/mL, with a notable limit of detection (LOD) of 1 pg/mL [12]. Wang *et al.* experimentally fabricated a tapered optical fiber and analyzed using LSPR technique for realizing a p-cresol biosensor. They extensively studied the stability, selectivity, and reusability test of the fabricated sensor, and finally achieved a remarkable sensitivity and LOD of 5.6 nm/mM, and 57.43 μM respectively [13]. Li *et al.* reported a creatinine biosensor designed with single-mode fiber-multicore fiber-multimode fiber-single-mode fiber. The sensor probe is functionalized with graphene oxide, gold nanoparticles and MoS_2 to boost the specificity and biocompatibility. They accomplished a sensitivity of 0.0025 nm/μM, and a LOD of 128.4 μM over a linear detection range of 0 - 2000 μM [14]. Later, in 2022, M. Li and his team experimentally developed an optical fiber sensor probe based on the LSPR technique for the detection of creatinine in aquaculture. The sensor probe is functionalized with MXene material in order to enhance the sensitivity and LOD [15]. Maji *et al.* reported a metal-distributed Bragg reflectors, where they studied the self-reference characteristics of the structure to investigate TPP modes for detecting the refractive index of different blood components and achieved a sensitivity of 200 nm/RIU [16]. Ahmed *et al.* studied TPP modes in a prism/Ag/$(LiNbO_3/SiO_2)^N$ configuration to sense temperature in the range 300K-700K in the NIR wavelength regime. By optimizing the thickness of various layers and incident angle, the authors realized a maximum sensitivity of 1.10 nm/K [17]. Qin *et al.* studied a planar multilayer Au integrated DBR structure using Tamm plasmon resonance technique for realization of narrowband and full-angle refractive index sensor. The authors achieved a sensitivity of only 860 nm/RIU and figure of merit of 391, which can be improved by replacing the conventional metal (Au) with the emerging 2D materials [18]. Kumar *et al.* demonstrated a metal-cavity-1D PhC configuration, for refractive index sensing application [19]. In this ref., the authors have not investigated the electric field intensity, absorption spectrum, and quality factor of the sensor, which demands further research.

With the rapid advancement in research on material science, numerous 2D materials such as graphene, WS_2, MoS_2, $PtSe_2$, black phosphorous, and phase change material (PCM) have been explored and integrated with existing photonic devices for sensing applications [20]–[23]. In this article, we propose a new class of 2D material known as MXene, and explore its metallic behavior to excite TPP modes at NIR wavelengths. MXene material exhibits certain extraordinary properties like strong carrier confinement [24], higher binding energy, excellent stability [25], narrow band gap [26], and notable hydrophilicity [27]. Recently, MXene has been the center of attraction for designing highly sensitive SPR sensors [28], [29]. Moreover, MXene can be synthesized using chemical vapor deposition (CVD) methods, hydrothermal synthesis, and alkali etching methods [30], [31].

While focusing on maximizing the sensitivity and quality factor, it should be noted that it is also vital to maintain a high sensing accuracy. With reference to refractive index sensing, external environmental factors like fluctuation in temperature and light intensity can adversely affect the sensing accuracy of identifying a single signal to measure the change in refractive index [32], [33]. For example, an extra resonant mode is formed in the spectral characteristics, which is very little impacted by the variation in the analyte concentrations. In this case, the extra resonant mode acts as reference signal. By analysis the reference signal, it is possible to decide whether the characteristics of the signal changes due to the change in the analyte concentrations. In this process, the errors of the sensing signal can be largely reduced, which ensures the high sensing accuracy. To meet the demand of high precision sensors, it is essential to study the self-reference characteristics in refractive index sensing [34], [34]–[36].

The present research has considerable novelty compared to the previously published similar works. To the best of our knowledge, so far the TPP modes have been studied only by considering the conventional plasmonic metals like Ag, Au and Al [37]. On the contrary, we have investigated the TPP modes using a 2D material Ti_3C_2Tx MXene, as a replacement to the traditional metals, which has not been reported earlier. Moreover, the self-reference characteristics of the designed sensor is thoroughly studied. The proposed structure is judiciously optimized for a new application, i.e. for detection of AIV H5N1 in poultry, which has not been highlighted before. Besides, the electric field distribution in

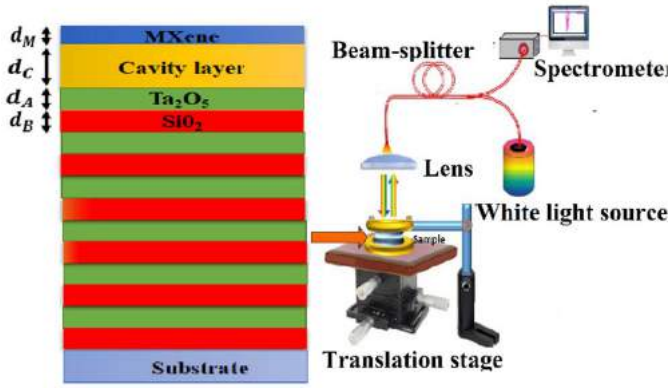

Fig. 1. (a) Schematic representation of MXene-1D PhC TPP structure (b) proposed experimental setup for realizing refractive index measurement scheme.

the structure is meticulously scrutinized by the colormap plot, which ensures the uniqueness of this work. A detailed analysis of reflection spectrum, absorption spectrum, and electric field intensity are carried out with respect to different concentrations of AIV H5N1. On top of that, we have compared the sensitivity and electric field intensity of the proposed MXene-based sensor with the traditional Ag-based sensor. Also, a comparative analysis is presented to confirm the significance of the designed sensor.

II. Proposed Geometry and Theoretical Modeling

The schematic of the proposed Ti_3C_2Tx MXene coated 1D PhC structure is illustrated in fig. 1(a). In particular, the 1D structure is comprised of alternate arrangements of dielectric layers of Ta_2O_5 and SiO_2. A cavity is inserted between the MXene layer and PhC, which is filled with liquid form of the poultry swab sample containing AIV H5N1. The 1D PhC is supported by a Si substrate at the end face. The thickness of different layers such as Ta_2O_5, SiO_2, MXene and cavity layer is denoted as d_A, d_B, d_M and d_C respectively. We assume normal incidence of the TE polarized light onto the structure. A schematic of the experimental setup for realization of the proposed sensor is shown in fig. 1(b). Fiber coupled white light source is incident on the proposed architecture, and the reflected light is collected by the same fiber which is then sent to the spectrometer. Further, the signal characteristics can be measured and recorded in a personal computer. In order to envisage the refractive-index sensitivity of the configuration supporting the TPP mode, the proposed structure could be mounted on a translation stage as shown in fig.1 (b). This arrangement enables changing the analyte refractive index and carrying out alteration in cavity layer thickness independent of each other.

The complex refractive index of MXene is computed experimentally at different thicknesses of 14 nm, 27 nm, and 75 nm in the visible-NIR wavelength region. The real (n) and imaginary part (k) of the complex refractive index is measured ellipsometrically by following the Tauc-Lorentz model. The

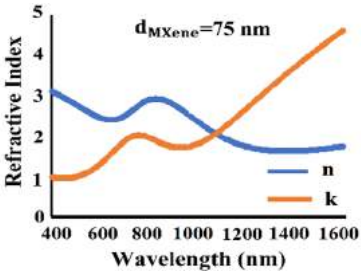

Fig. 2. Experimentally evaluated complex refractive index of MXene.

TABLE I
Refractive Index of Multilayer MXene at Different Thicknesses

MXene thickness (nm)	Refractive index (n+ki)	Wavelength (nm)
14	1.293+3.045i	1550
27	1.554+3.628i	
75	1.678+3.963i	

wavelength dependent refractive index of MXene at a thickness of 75 nm is delineated in fig. 2. The refractive index of MXene at other thicknesses (14 nm and 27 nm) is also computed, but not shown in the manuscript to simplify the same. However, we have mentioned the refractive index for different thicknesses at the reference wavelength of 1550 nm in table I. Also, we have validated our findings by comparing with the outcomes of the ref. [38].

The refractive indices of the constituent materials (SiO_2 and Ta_2O_5) of the PhC are computed by using the following equations [39], [40],

$$n_{Ta_2O_5} = 2.06 + \frac{0.024}{\lambda^2} \tag{1}$$

$$n_{SiO_2} = \sqrt{1 + \frac{A\lambda^2}{\lambda^2 - D^2} + \frac{B\lambda^2}{\lambda^2 - E^2} + \frac{C\lambda^2}{\lambda^2 - F^2}} \tag{2}$$

where, A=0.6961663, B=0.4079426, C=0.8974794, D=0.0684043, E=0.1162414, F=9.896161 are the Sellmeier coefficients.

To explore the reflection characteristics of the incident EM wave, we manipulate the well-established transfer matrix method (TMM) by considering the propagation of waves along the x-direction. The TMM describes the individual layer s in the form of a characteristics matrix M_s, which can be stated as [28],

$$M_s = \begin{bmatrix} cos\sigma_s & \left(-\frac{i}{\emptyset_s}\right) sin\sigma_s \\ -i\emptyset_s sin\sigma_s & cos\sigma_s \end{bmatrix} \tag{3}$$

For TE mode, the term σ_s and $\emptyset_s$ are defined as [28],

$$\sigma_s = \frac{2\pi}{\lambda} d_s n_s cos\theta_s \ \ and \ \ \emptyset_s = n_s cos\theta_s \tag{4}$$

where,d_s, n_s and θ_s denote the thickness, refractive index and angle of the incident light of the s^{th} layer. The transfer matrix of the entire geometry is computed by multiplying

the characteristics matrix of each layer, which can be stated as [41],

$$M = M_{MXene} M_{Cavity} (M_A M_B)^N = \begin{bmatrix} M(1,1) & M(1,2) \\ M(2,1) & M(2,2) \end{bmatrix} \tag{5}$$

The reflection coefficients can be computed using the elements of the transfer matrix M, which is expressed as [28],

$$r = \frac{(M(1,1) + M(1,2)\gamma_{su})\,\gamma_0 - (M(2,1) + M(2,2)\gamma_{su})}{(M(1,1) + M(1,2)\gamma_{su})\,\gamma_0 + (M(2,1) + M(2,2)\gamma_{su})} \tag{6}$$

In equation (6), γ_0 and γ_{su} are the parameters for initial medium (air) and final medium (substrate) respectively, which can be expressed as $\gamma_0 = \sqrt{\mu_0/\varepsilon_0} n_0 cos\theta_{in}$ and $\gamma_{su} = \sqrt{\mu_0/\varepsilon_0} n_{su} cos\theta_{su}$.

Lastly, the reflectance (R) of the proposed structure can be numerically expressed as [41],

$$R = |r|^2 \tag{7}$$

Absorption (A) of the structure is related to the transmittance (T) and reflectance (R) by the following expression [45],

$$A = 1 - T - R \tag{8}$$

Next, we discuss the essential dispersion conditions for generating the Tamm state in the cavity layer, and dielectric A and B of the PhC. The transitional interactions of the EM fields near the interface can be expressed as [42],

$$T_A = \begin{bmatrix} 1 & 1 \\ k_{Ax} & -k_{Ax} \end{bmatrix}, T_B = \begin{bmatrix} 1 & 1 \\ k_{Bx} & -k_{Bx} \end{bmatrix} \tag{9}$$

The terms k_{Ax} and k_{Bx} denote the x-component of the wave vector in the A and B layers respectively. The phase relationship of EM waves in the layers A (P_A) and B (P_B) can be given as [42],

$$P_A = \begin{bmatrix} e^{ik_{Ax}d_A} & 0 \\ 0 & e^{-ik_{Ax}d_A} \end{bmatrix} \tag{10}$$

$$P_B = \begin{bmatrix} e^{ik_{Bx}d_B} & 0 \\ 0 & e^{-ik_{Bx}d_B} \end{bmatrix} () \tag{11}$$

The connections between different layers can be accomplished by employing TMM, which can be written as follows [28],

$$Q = \begin{bmatrix} Q(1,1) & Q(1,2) \\ Q(2,1) & Q(2,2) \end{bmatrix} = T_B P_B T_B^{-1} T_A P_A T_A^{-1} \tag{12}$$

Finally, the dispersion equation of the Tamm state can be stated as [42],

$$\cos\delta_{D1} - i\frac{k_{D1x}}{k_{0x}} \sin\delta_{D1} + \left[\frac{\cos\delta_{D1}}{k_{0x}} - i\frac{\sin\delta_{D1}}{k_{D1x}}\right] \times \frac{\exp(iKd) - Q(1,1)}{Q(2,2)} = 0 \tag{13}$$

Here, K is the Bloch wave along the x-direction, $d = d_A + d_B$ and $\delta_{D1} = k_{D1x} \times d_{D1}$. It is essential to satisfy eq. (13) in order to produce Tamm state in the cavity layer.

It is indispensable to find performance parameters such as sensitivity, quality factor (Q), and detection limit (DL) of the proposed sensor to determine its degree of precision in detecting the small change in concentrations of AIV H5N1. Sensitivity (S) is defined as the ratio of the shift in TPP mode resonant wavelength ($\Delta\lambda_{res}$) to the corresponding change in concentrations (ΔC). Quality factor is the sensor potential to precisely detect the wavelength of the TPP mode resonance dips. DL is the ability of the sensor to detect the smallest shift in concentrations of AIV H5N1. Sensitivity, Q, and DL can be expressed mathematically as below [41], [43],

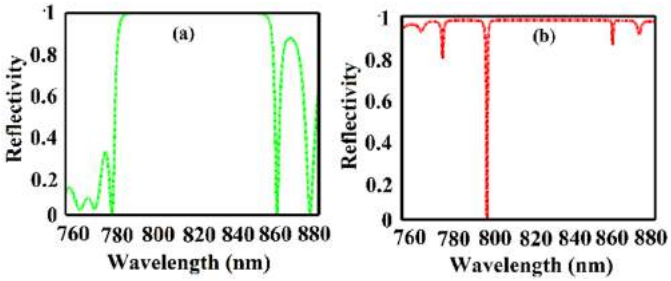

Fig. 3. Normal incidence reflection spectrum of the proposed structure (a) absence of MXene (b) presence of MXene.

$$S = \frac{\Delta\lambda_{res}}{\Delta C}, Q = \frac{\Delta\lambda_{res}}{FWHM}, and DL = \frac{R}{S} \tag{14}$$

Here, FWHM represents the full width half maximum of the TPP resonance mode and R denotes the resolution of the sensor.

III. Results and Discussions

With an aim to effectively and timely detect the AIV H5N1 virus in humans and animals, we propose a new configuration of TPP sensor. Refractive index is considered as the most important biophysical parameter to detect analyte concentrations. We have considered different concentrations (HAU) of H5N1 virus like 0.128, 0.32, 0.64, 0.96, 1.28 and 12.8, and their corresponding refractive index data are taken from ref. [44]. Initially, we select the geometrical parameters as $d_A = 185nm$, $d_B = 90nm$, $d_M = 75nm$, $d_C = 500nm$ and N=6. Fig. 3 shows the reflection spectra of the proposed structure before and after deposition of the MXene layer. In the absence of the MXene layer (fig. 3(a)), a band gap is observed in the range 766.8 nm to 897.2 nm with a width of 130.4 nm. On the other hand, with inclusion of the MXene layer (fig. 3(b)), it is noticed that the width of the band gap is significantly increased. Besides, a transverse localized TPP mode (sharp dip) is created at 797.4 nm, which is located within the PBG of the PhC. The appearance of this sharp dip is due to the excitation of TPP mode by the MXene layer. An elementary condition for the presence of the Tamm resonance is $r_{MXene} r_{PhC} = 1$, while the phase approaches to zero [45]. The resonance dip signifies that the light wavelength which is in resonance with TPP Eigen wavelength will pass through the structure, whereas other wavelengths of light will be prohibited from entering the structure. The position (wavelength) of the resonance dip is very sensitive to a small change in the refractive index of the cavity layer. Apart from the dominant TPP mode (797.4 nm), other modes with low intensity can be marked in the reflectance spectrum.

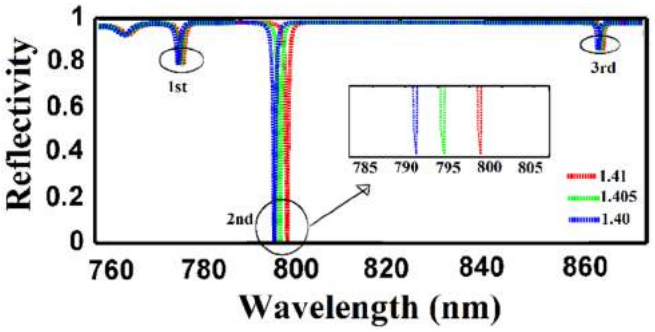

Fig. 4. Reflection spectrum for different analyte refractive index.

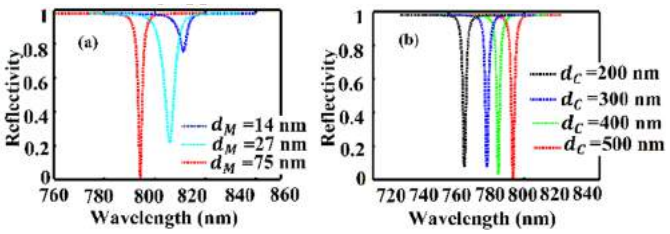

Fig. 5. Reflection spectrum at different thicknesses of (a) MXene layer (b) cavity layer for H5N1 concentration of 0.128 HAU.

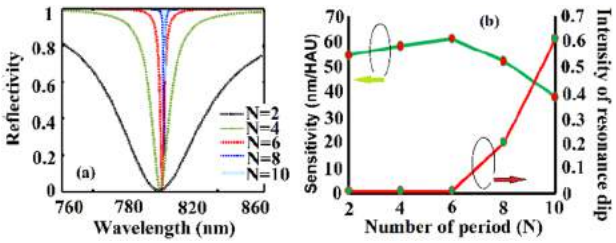

Fig. 6. Optimization of number of period (N) of the PhC.

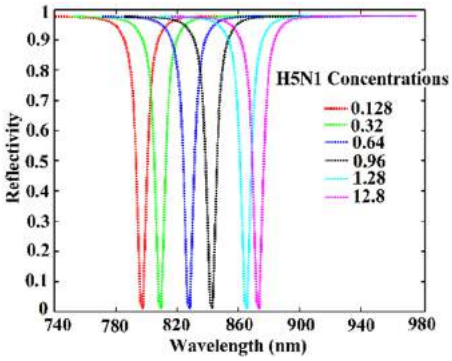

Fig. 7. The reflectance of the proposed structure at different concentrations of AIV H5N1.

Fig. 4 illustrates the shift in the three TPP resonant modes (marked as 1st, 2nd and 3rd) with change in refractive index (RI) of the cavity layer from 1.41 to 1.40. These refractive indices are taken only for testing the self-reference characteristics of the device. It is observed that with the change in RI of the analyte environment, only the 2nd resonant mode undergoes a notable shift from 797.4 nm to 791.6 nm (as shown in the inset graph), whereas the 1st and 3rd resonant modes are negligibly shifted with change in the analyte RI. Therefore, the 2nd TPP mode is quiet sensitive to change in the RI, which is useful for envisaging sensing applications. On the other hand, the 1st and 3rd TPP modes are insensitive to RI change, and act as reference signal. These reference modes are suitable to monitor the environmental factors like change in the temperature, fluctuations in the light intensity etc. In the subsequent analysis, we have studied the characteristics of only the 2nd TPP mode to realize the sensing application.

It is vital to analyse the effect of different thicknesses of the MXene layer and cavity layer to realize high performance. We optimized these thickness values through the analysis of the reflection spectrum which is plotted in fig. 5. At a constant cavity thickness (d_C) of 500 nm, the TPP resonance dip is blue-shifted (i.e. moved towards lower wavelength) with an increase in the thickness of MXene layer (d_M) from 14 nm to 27 nm to 75 nm as indicated in fig. 5 (a). Besides, the reflection intensity is decreased from 0.763 to 0.201 to 0.011 with the aforementioned change in thickness. The lowest reflection intensity of 0.011 at $d_M = 75nm$, indicates a maximum coupling between the incident light and TPP mode. Additionally, the TPP resonance peak appears sharper and thinner at the thickness of 75 nm, which specifies high sensor performance owing to the high value of figure of merit, quality factor, and detection limit. Therefore, we selected $d_M = 75nm$ as the optimized thickness of the MXene layer. Fig. 5 (b) shows the effect of change in the cavity thickness (d_C) on the reflection spectrum at $d_M = 75nm$. With an increase in d_CdC from 200nm to 500 nm, the reflection intensity of the resonance dip decreases from 0.07 to 0.011. We observed that the effect of change in d_CdC is comparatively less dominant than that of (d_M)dM. However, it is preferred to select cavity layer of higher thickness from fabrication point of view. So, we selected $d_C = 500$nm as the optimized value.

The number of period (N) of the PhC can significantly impact the reflection characteristics, intensity of the TPP resonance dip, FWHM, and sensitivity of the sensor. The value of N must be properly optimized such that the incoming and outgoing light coupling to the TPP mode exactly balances the Joule loss in the MXene layer [15]. Fig. 6 (a) illustrates the effect of different values of N on the reflection spectrum. Here, it can be noticed that for N=2 and N=4, the FWHM of the spectrum is relatively higher, which degrades the sensor performance. Although for N=8 and N=10 the FWHM is lower, but the intensity of the resonance dip (in the reflection spectrum) is higher which makes it difficult to detect the accurate resonance wavelength. Moreover, we found that for N=6, favorable value of FWHM and resonance dip intensity are achieved. From fig. 6 (b), it is clear that the sensitivity varies non-linearly with an increase in value of N from 2 to 10. A maximum sensitivity of 60.9375 nm/HAU is achieved at N=6. Further, it is observed that a feeble resonant dip intensity of 0.011 is obtained at N=6. Besides, for higher values of N (N>6), sensitivity decreases, and the intensity of resonant dip increases. So, N=6 is chosen as the optimized value to envisage high performance.

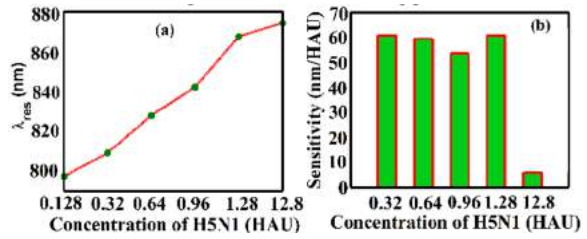

Fig. 8. (a) Shift in resonance wavelength (b) Sensitivity analysis.

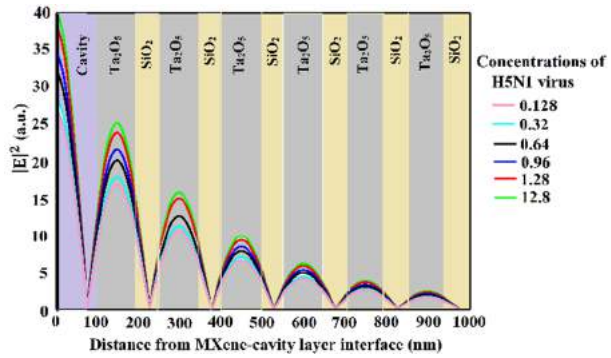

Fig. 9. Mode-field intensity distribution in the proposed structure for different H5N1 concentrations.

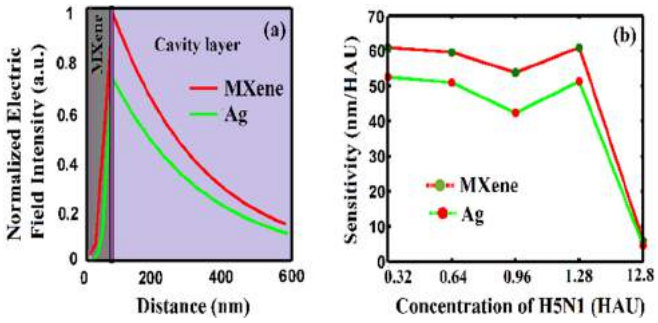

Fig. 10. Comparison of MXene and Ag based structure (a) normalized field intensity with respect to distance from MXene layer (b) sensitivity.

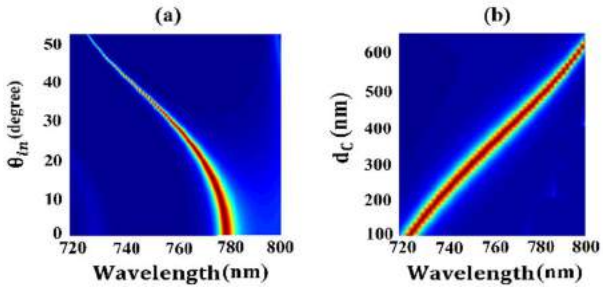

Fig. 11. Colormap plot (a) variation of resonant wavelength with respect to incident angle (b) variation of resonant wavelength with respect to thickness of the cavity layer.

Afterwards, we infiltrated the cavity region with various concentrations of AIV H5N1 and investigated the reflectance spectrum at $d_M = 75nm$, $d_C = 500nm$, and N=6, which is depicted in fig. 7. It is affirmed that with the increase in concentration of H5N1virus, the resonance dip is red-shifted to higher wavelength. As the concentration increases from 0.128 HAU to 12.8 HAU, the resonance dip is moved from 797.8 nm to 874.2 nm. As higher concentrations of virus correspond to higher refractive index, so the effective refractive index of the entire structure is modified which causes the red-shift in resonance dip. Moreover, this red-shifting nature of the resonance wavelength satisfies the Bragg's condition [46].

Fig. 8 (a) delineates the nature of variation of TPP mode resonance wavelength (λ_{res}) for different concentrations (C) of AIV H5N1. The figure elucidates that $\lambda_{res}\lambda_{\text{res}}$ increases almost linearly with change in virus concentrations. The variation can be mathematically expressed with a linear fitted equation, which is given as,

$$\lambda_{res} = 779.03 + 16.383 \times C \tag{15}$$

Fig. 8 (b) demonstrates the sensitivity analysis of the proposed sensor for different concentrations of AIV H5N1 (considering the concentration 0.128 HAU as the reference). The sensor delivers a maximum sensitivity of 60.937560.9375 nm/HAU, which is equivalent to 1.01×10^5 nm/RIU (by considering the change in the refractive index of different concentrations of H5N1). Thus, the proposed sensor can be viewed as a promising candidate for precise detection of different concentrations of H5N1 virus.

We investigated the tangential electric field distribution of light at the resonance dip wavelength for different concentrations of H5N1 virus. As depicted in fig. 9, the field intensity is maximum in the cavity layer, and gradually decays in an oscillating fashion away from it in the Ta_2O_5/SiO_2PhC structure. The high mode-field intensity in the cavity layer indicates more interaction of electric field with the infiltrated analyte which in-turn boost the sensing performance. Moreover, the peak electric field intensity decreases with increase in concentrations of H5N1 virus.

To prove the effectiveness of MXene as a metal, we compared the outcomes of the MXene-based structure with the traditional Ag-based structure, which is illustrated in fig. 10. Fig. 10 (a) shows the normalized electric field intensity (EFI) excited by the metal layer. The EFI reaches maximum value at the interface of metal-cavity layer and further exponentially decreases with increase in distance. It is observed that a maximum EFI of 0.98 is attained for MXene and 0.7 for Ag-based structure. So, the EFI increases by 40% in the case of MXene-based structure, which indicates more interaction of the electric field with the infiltrated analyte in the cavity layer. Fig. 10 (b) represents the sensitivity analysis of different concentrations of H5N1 virus in nm/HAU scale for both MXene and Ag-based structures. The maximum sensitivity of 60.937560.9375 nm/HAU and 52.5652.56 nm/HAU are obtained for MXene and Ag-based structure respectively. Here, it is declared that sensitivity increases by 15.93% if MXene is selected as the metal layer. Thus, the use of MXene as a plasmonic material can greatly enhance the sensor's performance.

As presented in fig. 11 (a), the TPP resonance wavelength decreases as the angle of incidence (θ_{in}) increases. So, the resonance dip undergoes a blue-shift for higher values of $\theta_{in}\theta_{\text{in}}$.

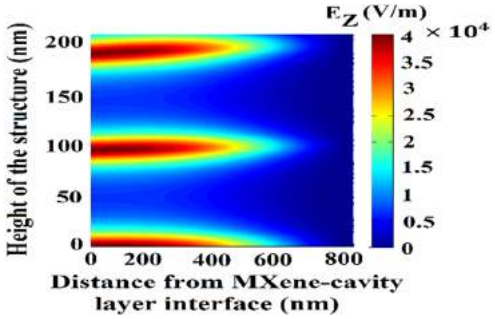

Fig. 12. Colormap plot of the electric field intensity distribution at the interface of MXene and cavity layer.

Besides, it is straightforward to ascertain that the peak position of the resonance slowly diverges from the center and inclines to the short-wavelength dip. Also, it is perceived that the intensity of the Tamm resonance dip decreases with increase in $\theta_{in}\theta_{\text{in}}$. The fundamental cause of blue-shift phenomenon can be described by Brag Snell's law [46],

$$m\lambda_{res} = 2N\sqrt{n_{eff}^2 - sin^2\theta_{in}} \tag{16}$$

Here, λ_{res} indicates the Tamm resonance wavelength, m represents the constructive diffraction order, N implies the period of the PhC, θ_{in} signifies the incident angle, n_{eff} denotes the effective refractive index.

Fig. 11 (b) depicts the colormap plot of change in Tamm resonance mode wavelength with respect to change in thickness of the cavity layer (d_c). It is marked that with the rise in d_c, the resonance dip possesses a red-shift (i.e. moves towards higher wavelengths). The primary cause of the aforementioned shift in resonant wavelength can be understood from standing wave condition [43]

$$\delta = p\lambda_{res} = n_{eff}\tau \tag{17}$$

where, δ and τ represent the optical and geometrical path difference respectively. The increase in the thickness of the cavity layer leads to increase in $\tau\tau$. In order to keep $\delta\delta$fixed, λ_{res} increases to higher value. This result is also in agreement with fig. 4(b).

Fig. 12 displays the electric field distribution for TE polarized light at the interface of MXene and cavity layer. It is seen that a high field intensity of 4×10^4 V/m is attained inside the cavity layer, which ensures the high coupling of EM waves with the infiltrated analyte. This effect leads to high absorption of analyte and better sensor performance. It is worth noting that the occurrence of high electric field intensity is due to the MXene layer, which is responsible for stimulating the TPP mode.

When a metal substrate (MXene) is integrated with 1D PhC, the resulting TPP modes provide strong light absorption. By employing TMM, the absorption spectrum of the proposed structure is investigated for different H5N1 concentrations and different thicknesses of the cavity layer (d_C), which are depicted in fig. 13 (a) and (b) respectively. It is evident that the MXene has a strong contribution of absorption to the overall absorption of the proposed multilayer structure. The

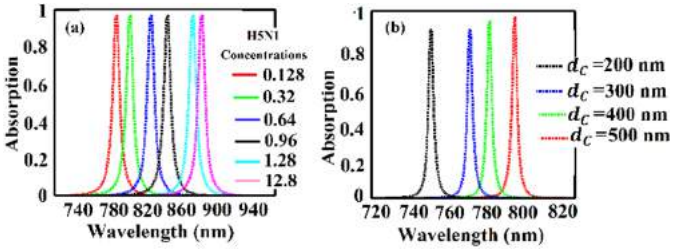

Fig. 13. Absorption spectrum of the proposed structure (a) for different concentrations of AIV H5N1 (b) for different values of d_C at H5N1 concentration of 0.128 HAU.

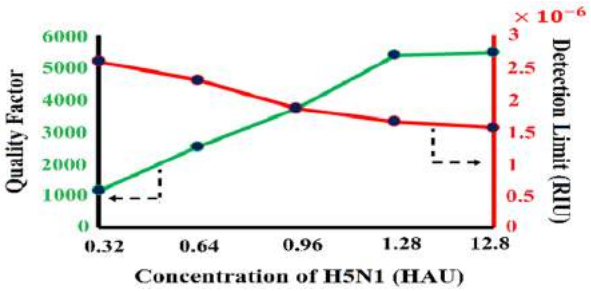

Fig. 14. Analysis of quality factor and detection limit.

TABLE II
COMPARATIVE ANALYSIS OF SENSING PARAMETERS

References	Configurations	Sensitivity (nm/RIU)	Q-factor	DL (RIU)
[25]	Ag/PSi-1D PhC	5018	2149.27	----
[37]	Ag/PSi annular PhC	6770	398	6.6×10^{-4}
[11]	Au-TiO_2/MgF_2 PhC	17	3000	0.88
[9]	Ag/1D DBR	10	300	----
This work	MXene/ (Ta_2O5/SiO_2) 1D PhC	1.01×10^5	5485.71	2.6×10^{-6}

absorption spectrum exhibits a sharp peak at the TPP resonant wavelength, which is due to the strongly localized electric field at λ_{res}. The peak absorption intensity approaches to unity and therefore, the transmission intensity is negligible. From fig. 12(a), it is noted that the absorption spectrum undergoes a noticeable red-shift (797.4 nm to 874.2 nm) with increase in the AVI H5N1 concentrations. The primary cause behind such shifts in absorption spectrum is the perceptible shift in the electric field distribution for different concentrations of H5N1 (as explained in fig. 8). From fig. 12(b), it is declared that the absorption spectrum is moved towards a higher wavelength (from 747 nm to 797.4 nm) with increase in d_Cd$_C$ (from 200 nm to 500 nm). It is seen that the peak of the absorption spectrum is increased with increase in d_Cd$_C$. At the optimized value of $d_C = 500$ nm, the maximum absorption is realized, which is in agreement with eq. (8).

Apart from sensitivity, we numerically computed other vital sensing parameters such as quality factor (Q) and detection limit (DL). From Fig. 14, it can be perceived that Q increases and DL decreases with respect to increase in the concentration of H5N1 virus. An optimum quality factor of 5485.71 and detection limit of 2.6×10^{-6} RIU are obtained for the proposed Tamm plasmon sensor, which can be considered as noteworthy sensing performances. Eventually, we compared the performance parameters of the proposed sensor with the recently published similar works, which is represented in table II. From this table, it can be perceived that the proposed sensor bestows superior performance vis-à-vis sensitivity, Q-factor, and DL.

IV. Conclusion

Recognizing the significance of accurate and timely detection of different concentrations of AIV H5N1 in humans and animals, we attempted to design a self-reference TPP refractive index sensor having configuration MXene/cavity/$(Ta_2O_5/SiO_2)^N$/substrate. The sensing principle is based on computing the shift in wavelength and intensity of the resonance dip, which is basically a consequence of TPP mode resonance at the MXene and 1D PhC. Different structure parameters like thickness of MXene material, thickness of the cavity layer, period of the PhC have been sensibly optimized. A sharp TPP resonance, which ensures high sensing performance, is obtained at the optimized structure parameters like Ta_2O_5 layer thickness $d_A = 185nm$, SiO_2 layer thickness $d_B = 90nm$, MXene layer thickness $d_M = 75nm$, cavity layer thickness $d_C = 500nm$, number of period N=6 and incident angle $\theta_{in} = 0^o$. Upon infiltrating the cavity layer with different concentrations of AIV H5N1 and employing TMM, we investigated the reflection spectrum, absorption spectrum and electric field intensity for each concentrations. We obtained an optimum sensitivity of 60.9375 nm/HAU, quality factor of 5485.71, and detection limit of 2.6×10^{-6} RIU for the proposed sensor, which can be considered as remarkable performance. More importantly, compared to the conventional Ag-based TPP sensor, the electric field intensity (EFI) and sensitivity of the proposed MXene-based TPP sensor have been boosted by 40% and 15.93% respectively. So, MXene can be regarded as a promising material to design new-age photonic sensors. Above all, the superiority of the designed sensor is verified by comparing the sensing outcomes with the recently published similar works. So, the proposed sensor can find suitable applications in the biomedical industry.

References

[1] J. Lum *et al.*, "Rapid detection of avian influenza H5N1 virus using impedance measurement of immuno-reaction coupled with RBC amplification," *Biosensors Bioelectron.*, vol. 38, no. 1, pp. 67–73, Oct. 2012.

[2] M. D. de Jong *et al.*, "Fatal outcome of human influenza a (H5N1) is associated with high viral load and hypercytokinemia," *Nature Med.*, vol. 12, no. 10, pp. 1203–1207, Oct. 2006.

[3] World Health Organization (WHO). *Global Influenza Programme*. Accessed: Oct. 20, 2021. [Online]. Available: https://www.who.int/teams/global-influenza-programme/avian-influenza

[4] J. M. Katz, "The impact of avian influenza viruses on public health," *Avian Diseases*, vol. 47, no. s3, pp. 914–920, Sep. 2003.

[5] T. Rowe *et al.*, "Detection of antibody to avian influenza a (H5N1) virus in human serum by using a combination of serologic assays," *J. Clin. Microbiol.*, vol. 37, no. 4, pp. 937–943, Apr. 1999.

[6] R. A. M. Fouchier, T. M. Bestebroer, S. Herfst, L. Van Der Kemp, G. F. Rimmelzwaan, and A. D. M. E. Osterhaus, "Detection of influenza a viruses from different species by PCR amplification of conserved sequences in the matrix gene," *J. Clin. Microbiol.*, vol. 38, no. 11, pp. 4096–4101, Nov. 2000.

[7] Y. Chen *et al.*, "Evaluation of a rapid test for detection of H5N1 avian influenza virus," *J. Virolog. Methods*, vol. 154, nos. 1–2, pp. 213–215, Dec. 2008.

[8] X. Zhang, X.-S. Zhu, and Y.-W. Shi, "Tamm plasmon polariton based hollow fiber refractive index sensor with one-dimensional photonic crystal/metal structure," *IEEE Sensors J.*, vol. 19, no. 7, pp. 2570–2575, Apr. 2019.

[9] G. Lheureux, "Tamm plasmons in metal/nanoporous GaN distributed Bragg reflector cavities for active and passive optoelectronics," *Opt. Exp.*, vol. 28, no. 12, pp. 17934–17943, 2020.

[10] S. I. Abbas *et al.*, "Studying of the polarization modes TE and TM for oblique incidence of light on thin films," *Dig. J. Nanomater. Biostruct.*, vol. 16, pp. 647–657, Apr. 2017.

[11] V. V. Klimov, A. A. Pavlov, I. V. Treshin, and I. V. Zabkov, "Fano resonances in a photonic crystal covered with a perforated gold film and its application to bio-sensing," *J. Phys. D, Appl. Phys.*, vol. 50, no. 28, Jul. 2017, Art. no. 285101.

[12] C. Leit?o *et al.*, "Cortisol AuPd plasmonic unclad POF biosensor," *Biotechnol. Rep.*, vol. 29, Mar. 2021, Art. no. e00587.

[13] Y. Wang *et al.*, "Water pollutants p-cresol detection based on Au-ZnO nanoparticles modified tapered optical fiber," *IEEE Trans. NanoBiosci.*, vol. 20, no. 3, pp. 377–384, Jul. 2021.

[14] M. Li, R. Singh, C. Marques, B. Zhang, and S. Kumar, "2D material assisted SMF-MCF-MMF-SMF based LSPR sensor for creatinine detection," *Opt. Exp.*, vol. 29, no. 23, pp. 38150–38167, 2021.

[15] M. Li, R. Singh, M. S. Soares, C. Marques, B. Zhang, and S. Kumar, "Convex fiber-tapered seven core fiber-convex fiber (CTC) structure-based biosensor for creatinine detection in aquaculture," *Opt. Exp.*, vol. 30, no. 8, pp. 13898–13914, Apr. 2022.

[16] P. S. Maji, M. K. Shukla, and R. Das, "Blood component detection based on miniaturized self-referenced hybrid Tamm-plasmon-polariton sensor," *Sens. Actuators B, Chem.*, vol. 255, pp. 729–734, Feb. 2018.

[17] A. M. Ahmed and A. Mehaney, "Novel design of wide temperature ranges sensor based on Tamm state in a pyroelectric photonic crystal with high sensitivity," *Phys. E, Low-Dimensional Syst. Nanostruct.*, vol. 125, Jan. 2021, Art. no. 114387.

[18] L. Qin, S. Wu, C. Zhang, and X. Li, "Narrowband and full-angle refractive index sensor based on a planar multilayer structure," *IEEE Sensors J.*, vol. 19, no. 8, pp. 2924–2930, Apr. 2019.

[19] S. Kumar, "Optical Tamm plasmon based biosensor in the near infrared region," in *Proc. Workshop Recent Adv. Photon. (WRAP)*, Dec. 2019, pp. 1–3, doi: 10.1109/WRAP47485.2019.9013729.

[20] A. Panda and P. D. Pukhrambam, "A theoretical proposal of high performance blood components biosensor based on defective 1D photonic crystal employing WS_2, MoS_2 and graphene," *Opt. Quantum Electron.*, vol. 53, no. 7, p. 357, Jul. 2021.

[21] A. Panda, P. D. Pukhrambam, and G. Keiser, "Performance analysis of graphene-based surface plasmon resonance biosensor for blood glucose and gas detection," *Appl. Phys. A, Solids Surf.*, vol. 126, no. 3, p. 153, Mar. 2020.

[22] A. Panda, D. Vigneswaran, P. D. Pukhrambam, N. Ayyanar, and T. K. Nguyen, "Design and performance analysis of reconfigurable 1D photonic crystal biosensor employing $Ge_2Sb_2Te_5$ (GST) for detection of women reproductive hormones," *IEEE Trans. Nanobiosci.*, vol. 21, no. 1, pp. 21–28, Jan. 2022.

[23] A. Panda and P. D. Pukhrambam, "Modeling of high-performance SPR refractive index sensor employing novel 2D materials for detection of malaria pathogens," *IEEE Trans. Nanobiosci.*, vol. 21, no. 2, pp. 312–319, Apr. 2022.

[24] X. Jiang *et al.*, "Broadband nonlinear photonics in few-layer MXene $Ti_3C_2T_x$ (T = F, O, or OH)," *Laser Photon. Rev.*, vol. 12, Feb. 2018, Art. no. 1700229.

[25] X.-F. Yu *et al.*, "Monolayer Ti_2CO_2: A promising candidate for NH3 sensor or capturer with high sensitivity and selectivity," *ACS Appl. Mater. Interface*, vol. 7, no. 24, pp. 13707–13713, Jun. 2015.

[26] O. Salim, K. A. Mahmoud, K. K. Pant, and R. K. Joshi, "Introduction to MXenes: Synthesis and characteristics," *Mater. Today Chem.*, vol. 14, Dec. 2019, Art. no. 100191.

[27] S. Li, H. Li, Y. Zhou, and H. Zhai, "Mechanism for abnormal thermal shock behavior of Cr2AlC," *J. Eur. Ceram. Soc.*, vol. 34, no. 5, pp. 1083–1088, May 2014.

[28] A. Srivastava, A. Verma, R. Das, and Y. K. Prajapati, "A theoretical approach to improve the performance of SPR biosensor using MXene and black phosphorus," *Optik*, vol. 203, Feb. 2020, Art. no. 163430.
[29] Y. Xu, Y. Ang, L. Wu, and L. Ang, "High sensitivity surface plasmon resonance sensor based on two-dimensional MXene and transition metal dichalcogenide: A theoretical study," *Nanomaterials*, vol. 9, no. 2, p. 165, Jan. 2019.
[30] T. F. Li *et al.*, "Fluorine-free synthesis of high-purity $Ti_3C_2T_x$ (T=OH, O) via alkali treatment," *Angew. Chem. Int. Ed. Engl.*, vol. 57, no. 21, pp. 6115–6119, 2018.
[31] L. Wang *et al.*, "Synthesis and electrochemical performance of $Ti_3C_2T_x$ with hydrothermal process," *Electron. Mater. Lett.*, vol. 12, no. 5, pp. 702–710, Sep. 2016.
[32] R. Kohandani and S. S. Saini, "Self-referencing plasmonic array sensors," *Plasmonics*, vol. 15, no. 5, pp. 1359–1368, Oct. 2020.
[33] P. Sun *et al.*, "Self-referenced refractive index sensor based on hybrid mode resonances in 2D metal-dielectric grating," *J. Phys. D, Appl. Phys.*, vol. 53, no. 14, Apr. 2020, Art. no. 145101.
[34] X. Wang *et al.*, "A plasmonic refractive index sensor with double self-reference characteristic," *EPL Europhys. Lett.*, vol. 135, no. 2, Jul. 2021, Art. no. 27001.
[35] Y. Wang, C. Sun, H. Li, Q. Gong, and J. Chen, "Self-reference plasmonic sensors based on double Fano resonances," *Nanoscale*, vol. 9, no. 31, pp. 11085–11092, 2017.
[36] J. Zhu, X. Wang, Y. Qi, and J. Yu, "Plasmonic sensor with self-reference capability based on functional layer film composed of Au/Si gratings," *Chin. Phys. B*, vol. 31, no. 1, Jan. 2022, Art. no. 014206.
[37] A. Mehaney, M. M. Abadla, and H. A. Elsayed, "1D porous silicon photonic crystals comprising Tamm/Fano resonance as high performing optical sensors," *J. Mol. Liquids*, vol. 322, Jan. 2021, Art. no. 114978.
[38] A. D. Dillon *et al.*, "Highly conductive optical quality solution-processed films of 2D titanium carbide," *Adv. Funct. Mater.*, vol. 26, no. 23, pp. 4162–4168, Jun. 2016.
[39] T. J. Bright *et al.*, "Infrared optical properties of amorphous and nanocrystalline Ta_2O_5 thin films," *J. Appl. Phys.*, vol. 114, Aug. 2013, Art. no. 083515.
[40] *Refractive Index of SiO_2 (Silicon Dioxide, Silica, Quartz)*, Malitson, Sydney, NSW, Australia, 1965.
[41] A. Panda and P. D. Pukhrambam, "Investigation of defect based 1D photonic crystal structure for real-time detection of waterborne bacteria," *Phys. B, Condens. Matter*, vol. 607, Apr. 2021, Art. no. 412854.
[42] B.-F. Wan, Z.-W. Zhou, Y. Xu, and H.-F. Zhang, "A theoretical proposal for a refractive index and angle sensor based on one-dimensional photonic crystals," *IEEE Sensors J.*, vol. 21, no. 1, pp. 331–338, Jan. 2021.
[43] A. Panda, P. D. Pukhrambam, F. Wu, and W. Belhadj, "Graphene-based 1D defective photonic crystal biosensor for real-time detection of cancer cells," *Eur. Phys. J. Plus*, vol. 136, no. 8, p. 809, Aug. 2021.
[44] H. Bai, R. Wang, B. Hargis, H. Lu, and Y. Li, "A SPR aptasensor for detection of avian influenza virus H5N1," *Sensors*, vol. 12, no. 9, pp. 12506–12518, Sep. 2012.
[45] A. Juneau-Fecteau, R. Savin, A. Boucherif, and L. G. Fréchette, "A practical Tamm plasmon sensor based on porous Si," *AIP Adv.*, vol. 11, no. 6, Jun. 2021, Art. no. 065305.
[46] A. Panda, P. D. Pukhrambam, N. Ayyanar, and T. K. Nguyen, "Investigation of transmission properties in defective one dimensional superconductive photonic crystal for ultralow level bioethanol detection," *Optik*, vol. 245, Nov. 2021, Art. no. 167733.

Abinash Panda (Graduate Student Member, IEEE) received the B.Tech. and M.Tech. degrees in electronics and communication engineering from the Biju Patnaik University of Technology (BPUT), Odisha, India. Currently, he is pursuing the Ph.D. degree with the National Institute of Technology, Silchar, Assam, India. His research interests include photonic waveguides, photonic crystals, biophotonic sensors, plasmonic sensors, and optoelectronic devices.

Puspa Devi Pukhrambam (Member, IEEE) received the B.Tech. degree in electronics and communication engineering from the North Eastern Regional Institute of Science and Technology, and the M.S. and Ph.D. degrees in electronics and computer engineering from the National Taiwan University of Science and Technology (NTUST), Taipei, Taiwan. She is currently an Assistant Professor with the Electronics and Communication Engineering Department, National Institute of Technology, Silchar, Assam, India. Her current research interests include semiconductor optoelectronic devices, optical networking, III-V semiconductors, plasmonic sensors, and electronic biosensors.

Joni Welman Simatupang (Senior Member, IEEE) received the B.E. degree from the University of Indonesia, and the M.Sc. and Ph.D. degrees in electronics and computer engineering from the National Taiwan University of Science and Technology (NTUST), Taipei, Taiwan. He is currently an Associate Professor with the Electrical Engineering Department, President University, Indonesia. His current research interests include photonics communications, optical fiber sensors (OFS), semiconductor devices, power electronics, the IoT, and optoelectronic sensors.